Microwave response and surface impedance of weak links

J. McDonald and John R. Clem
Ames Laboratory and Department of Physics and Astronomy, Iowa State University, Ames, Iowa 50011
(Received 7 May 1997)

The behavior of superconducting weak links in an ac magnetic field is considered. Both small and long uniform junctions are analyzed. Analytical results are presented for various limiting cases. The general case is solved numerically for different parameter choices and the results are presented. Both similarities and significant differences are found between the small junction and the long uniform junction. [S0163-1829(97)02845-2]

I. INTRODUCTION

The response of Josephson junctions to ac disturbances has been the subject of an enormous amount of research over the last several decades. Shapiro steps,[1] I-V characteristics,[2,3] and chaos[4,5] have been extensively studied both experimentally and theoretically.

The microwave response of superconducting weak links continues to be of considerable interest at the present time.[6–9] Much of this interest stems from the desire to use high-temperature superconductors (HTS's) in passive microwave devices such as filters for wireless communication.[10–13] Samples of HTS's are often granular in composition, consisting of superconducting grains coupled to one another by grain-boundary junctions.[14] This granularity leads to nonlinear effects such as harmonic generation (HG) and two-frequency intermodulation (IM), and also to a dependence of the surface impedance on the amplitude of the ac field.[15,16] These nonlinearities can cause various problems in device applications. One consequence of the field dependence is that the low-power surface impedance is no longer a sufficient figure of merit. Instead, the surface impedance must be determined at the specific power at which the device will be operated.[17] The occurrence of IM in filters can cause problems such as the generation of spurious targets in radar receivers.[17] A thorough understanding of all these nonlinear effects is essential before high-quality devices can be designed and constructed. Nonlinear effects characteristic of uniform Josephson junctions have also been reported recently in single crystals of $Bi_2Sr_2CaCu_2O_8$ and $YBa_2Cu_3O_{6.95}$.[6,7]

Josephson effects and granularity in HTS's have been modeled previously by various authors. Clem,[18] Dersch and Blatter,[19] Tinkham *et al.*,[20,21] and Sonin and Tagantsev[22] have independently modeled a granular HTS as an array of weakly Josephson-coupled, strongly superconducting grains. A Ginzburg-Landau approach was employed in which the array was approximated as a continuous medium characterized by effective Ginzburg-Landau parameters (coherence length, penetration depth, critical fields, etc.). Analogies were then drawn between granular HTS's and ordinary type-II superconductors. Hylton *et al.*[23] treated the residual high-frequency losses in HTS's using a coupled-grain model in which the grains were taken to be purely inductive and the weak links were modeled using the resistively shunted junction (RSJ) model. This approach has been employed and expanded by various authors.[8,24–26] Halbritter has considered various regimes of the field, frequency, and temperature dependence of the surface impedance of HTS's.[27–29]

The purpose of this paper is to treat the nonlinear response of a single Josephson junction in an applied ac magnetic field. In Sec. II we treat the case of a small junction. The resistance, reactance, and third-order harmonic generation components are calculated as a function of the amplitude of the current flowing through the junction. In Sec. III the behavior of a long uniform junction is analyzed. In Sec. IV a brief review of previous work on Josephson junction arrays is given. The results of this paper are summarized in Sec. V.

II. SMALL, SINGLE JUNCTIONS

Penetration of magnetic flux into a Josephson junction occurs on a length scale characterized by the Josephson penetration depth λ_J. A Josephson junction is small if all its dimensions transverse to the magnetic field are smaller than λ_J. The ac properties of a junction satisfying this criterion are most easily treated using the resistively and capacitively shunted junction (RCSJ) model.[216,30] In this model the Josephson junction is modeled by an ideal junction J shunted by a resistance R and a capacitance C to form a parallel

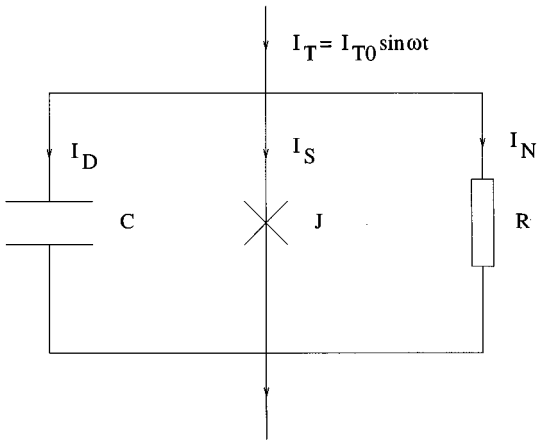

FIG. 1. The circuit used to represent an actual Josephson junction in the RCSJ model. An ideal junction J is shunted by a resistance R and a capacitance C. The transport current I_T flowing through the junction is the sum of three terms: a supercurrent I_S through the ideal junction, a normal current I_N through the resistance, and a displacement current I_D through the capacitance.

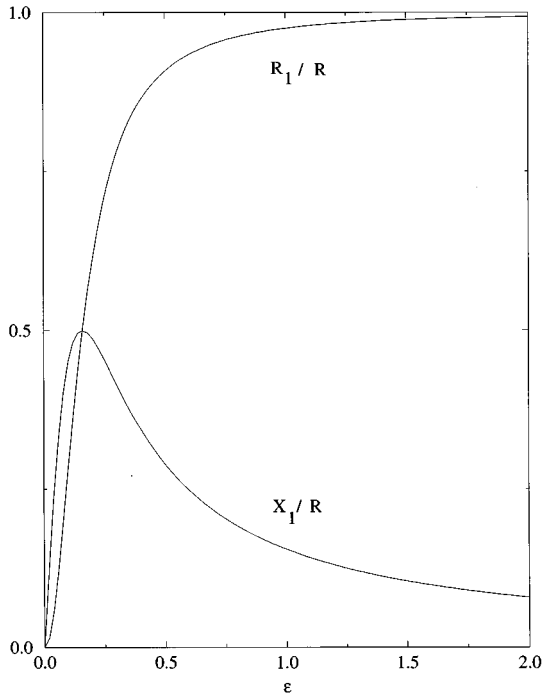

FIG. 2. The resistance R_1 and reactance X_1 vs ε for the RSJ model when $I \ll 1$ [see Eqs. (15) and (16)]. R_1 increases from zero quadratically with increasing ε and quickly approaches the shunting resistance R. X_1 initially increases linearly with increasing ε, goes through a maximum at $\varepsilon = 1/2\pi$, and then decreases to zero as $1/\varepsilon$ as $\varepsilon \to \infty$. When $\varepsilon = 1/2\pi$ the shunting resistance is equal to the Josephson reactance ($R = \omega L_J = \phi_0 \omega / 2\pi I_0$), and $R_1 = X_1 = R/2$.

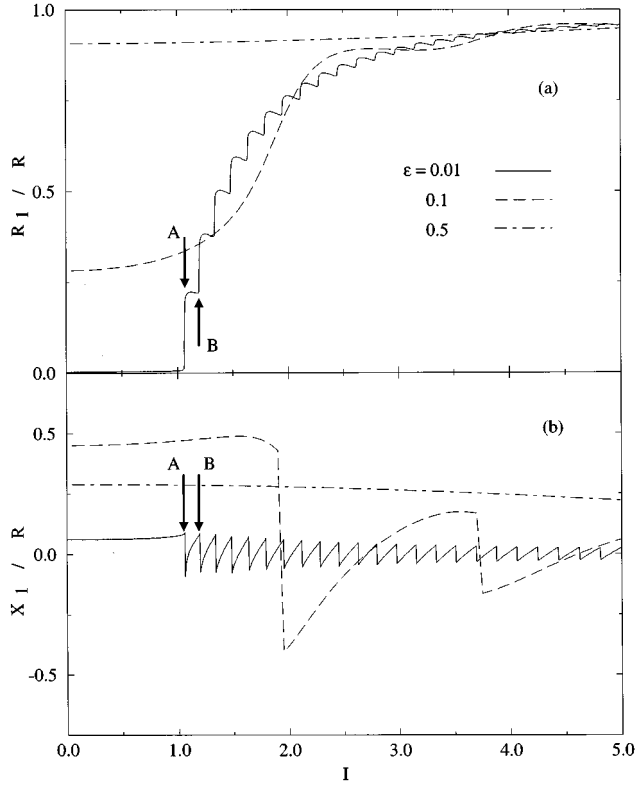

FIG. 3. The resistance R_1 (top) and reactance X_1 (bottom) vs I in the RSJ model for three different values of ε. When ε is small, there are very sharp jumps. These jumps occur because of bifurcations in the gauge-invariant phase difference $\Delta\gamma$. Arrows indicate jumps at values of I for which bifurcations in $\Delta\gamma$ versus t are illustrated in Fig. 5. As ε increases, the bifurcations move to larger values of I, and successive bifurcations are spaced further apart. This causes the sharp steps to become broadened, to become less frequent, and eventually to disappear completely.

circuit (see Fig. 1). The current flowing through the circuit, I_T, can be thought of as the superposition of a supercurrent I_S, a normal current I_N, and a displacement current I_D. The normal current is caused by the flow of quasiparticles across the junction, while the displacement current is due to the time-varying electric field between the superconducting electrodes. The supercurrent, which flows through the ideal junction, is given by the Josephson relation

$$I_S = I_0 \sin\Delta\gamma, \tag{1}$$

where I_0 is the critical current of the junction and $\Delta\gamma$ is the gauge-invariant phase difference across the junction. The normal current and the displacement current are given by

$$I_N = \frac{V}{R} \tag{2}$$

and

$$I_D = C\frac{d}{dt}V, \tag{3}$$

where V is the voltage drop across the junction. The relation between V and $\Delta\gamma$ is

$$V(t) = \frac{\phi_0}{2\pi}\frac{d}{dt}\Delta\gamma(t), \tag{4}$$

where $\phi_0 = h/2e = 2.07 \times 10^{-15}$ V s is the superconducting flux quantum. Combining Eqs. (1)–(4) yields

$$I_T = I_S + I_N + I_D = I_0 \sin\Delta\gamma(t) + \frac{\phi_0}{2\pi R}\frac{d}{dt}\Delta\gamma(t) + \frac{\phi_0 C}{2\pi}\frac{d^2}{dt^2}\Delta\gamma(t). \tag{5}$$

For a given transport current we can determine $\Delta\gamma(t)$ by solving Eq. (5). In microwave applications I_T typically varies sinusoidally, $I_T = I_{T0}\sin(\omega t)$. In this case Eq. (5) becomes

$$\frac{1}{4\pi^2}\left(\frac{\omega}{\omega_p}\right)^2\frac{d^2}{dt'^2}\Delta\gamma(t') + \varepsilon\frac{d}{dt'}\Delta\gamma(t') + \sin\Delta\gamma(t') = I\sin(2\pi t'), \tag{6}$$

where $t' = t/T = \omega t/2\pi$, $\omega_p = \sqrt{1/L_J C}$, $\varepsilon = \omega L_J/2\pi R$, $L_J = \phi_0/2\pi I_0$, and $I = I_{T0}/I_0$. The frequency ω_p is the plasma frequency of the junction. Equation (6) has been shown to have chaotic solutions in certain parameter regimes.[4,5] This can complicate the calculation of the surface

impedance because the solution can be aperiodic. For low driving frequencies $\omega \ll \omega_p$, Eq. (6) reduces to

$$\varepsilon \frac{d}{dt'}\Delta\gamma(t') + \sin\Delta\gamma(t') = I \sin(2\pi t'). \tag{7}$$

The steady-state solution of Eq. (7) is periodic in the variable t', with a period equal to 1. The voltage drop given by Eq. (3) will also be periodic with the same period. Therefore, we may expand V in a Fourier series,

$$V(t') = I_{T0}\sum_{n=1}^{\infty}[R_n \sin(2\pi n t') + X_n \cos(2\pi n t')], \tag{8}$$

where the coefficients are given by

$$R_n = \frac{2}{I_{T0}}\int_0^1 V(t')\sin(2\pi n t')dt' \tag{9}$$

and

$$X_n = \frac{2}{I_{T0}}\int_0^1 V(t')\cos(2\pi n t')dt'. \tag{10}$$

The coefficient R_1 is related to the time-averaged dissipated power $P_{\rm diss}$,

$$P_{\rm diss} = \int_0^1 I_T(t')V(t')dt' = \frac{1}{2}I_{T0}^2 R_1. \tag{11}$$

Equation (11) indicates that R_1 is the resistance. The coefficient X_1 is the reactance. For $n>1$ the coefficients are related to the generation of higher harmonics by the junction.

In the limit of small transport current, $I \ll 1$, $\Delta\gamma \ll 1$, and $\sin\Delta\gamma \simeq \Delta\gamma$. In this case Eq. (7) can be linearized,

$$\varepsilon \frac{d}{dt'}\Delta\gamma(t') + \Delta\gamma(t') = I \sin(2\pi t'). \tag{12}$$

The steady-state solution of Eq. (12) is

$$\Delta\gamma(t') = \frac{I}{1+4\pi^2\varepsilon^2}[-2\pi\varepsilon\cos(2\pi t') + \sin(2\pi t')], \tag{13}$$

and the resulting expression for $V(t')$ is

$$V(t') = I_{T0}R\frac{2\pi\varepsilon}{1+4\pi^2\varepsilon^2}[2\pi\varepsilon\sin(2\pi t') + \cos(2\pi t')]. \tag{14}$$

By comparing this with Eq. (8) one can see that

$$R_1 = \frac{4\pi^2\varepsilon^2}{1+4\pi^2\varepsilon^2}R \tag{15}$$

and

$$X_1 = \frac{2\pi\varepsilon}{1+4\pi^2\varepsilon^2}R. \tag{16}$$

These expressions are plotted as a function of ε in Fig. 2. There is a local maximum in X_1 at $\varepsilon = 1/2\pi$. At this value of ε the shunting resistance R is equal to the Josephson reactance ωL_J and $R_1 = X_1 = (1/2)R$.

In the opposite limit of large transport current, $I \gg 1$, $I_N \gg I_S$, and I_S can be neglected in Eq. (7),

$$\varepsilon \frac{d}{dt'}\Delta\gamma(t') = I \sin(2\pi t'). \tag{17}$$

The resulting $V(t')$ is

$$V(t') = I_{T0}R \sin(2\pi t'), \tag{18}$$

which implies $R_1 = R$ and $X_1 = 0$. This is also the solution when $\varepsilon \gg 1$.

In general, however, Eq. (7) must be solved numerically. This has been done previously by various authors.[8,9,31–33] Figure 3(a) shows R_1 versus I for three different values of ε. When $\varepsilon \ll 1$, there are very sharp steps in R_1 for $I>1$ (A and B, for example). Corresponding steps also are seen in X_1, R_3, and X_3 for small ε, as shown in Figs. 3(b), 4(a), and 4(b), respectively. For R_1, the step heights decrease in magnitude with increasing I, and when $I \gg 1$, $R_1 \simeq R$, as expected. The sharp steps occur at values of I for which there are bifurcations in the solutions of Eq. (7). Figure 5(a) shows the first two bifurcations (marked A and B in Figs. 3 and 4) for $\varepsilon = 0.01$. These bifurcations cause sudden changes in the voltage drop $V(t)$ given in Eq. (4). As shown in Fig. 5(b), for $I = 1.064$ there is a negative voltage pulse near $t' = 0.4$ and a positive voltage pulse around $t' = 0.9$, while for $I = 1.065$ there is positive pulse near $t' = 0.4$ and a negative one near $t' = 0.9$. The voltage responses at $I = 1.198$ and $I = 1.199$ also differ from each other by a change in sign of voltage pulses in the neighborhood of $t' = 0.4$ and $t' = 0.9$. Therefore, the sharp features in the curves of R_1, X_1, R_3, and X_3 correspond to the inversion of a voltage pulse at two different times during one cycle of the alternating current. As ε is increased, the bifurcations in the solution move to larger values of I, and the spacing between them becomes larger. The steps in R_1 are therefore broadened [see Fig. 3(a)]. As $\varepsilon \to \infty$, all the bifurcations are pushed to infinitely large values of I, and $R_1 \to R$. The curves in Fig. 3(a) indicate that this transition is approached quite rapidly.

III. LONG, UNIFORM JUNCTIONS

A Josephson junction is long if one of its dimensions transverse to the magnetic field is much larger than λ_J. In this case the RCSJ model no longer gives an adequate description of the ac properties of the junction.

Consider a semi-infinite superconductor ($x>0$) containing the junction pictured in Fig. 6. The entire region $x>0$, except for a slab of thickness d_i centered on the x-z plane, is occupied by a superconductor with London penetration depth λ. The slab consists of a nonsuperconducting material of resistivity ρ_i and permittivity ϵ. There is an applied field $\mathbf{B_a} = B_{a0}\sin(\omega t)\hat{z}$ in the region $x<0$. The Josephson penetration depth for this junction is $\lambda_J = \sqrt{\phi_0/(2\pi\mu_0 J_0 d)}$, where the magnetic thickness d is given by $d = 2\lambda + d_i$ and J_0 is the critical current density of the junction. The relation between the gauge-invariant phase difference across the junction $\Delta\gamma(x,t)$ and the magnetic field along the junction $b_z(x,t)$ is given by[21]

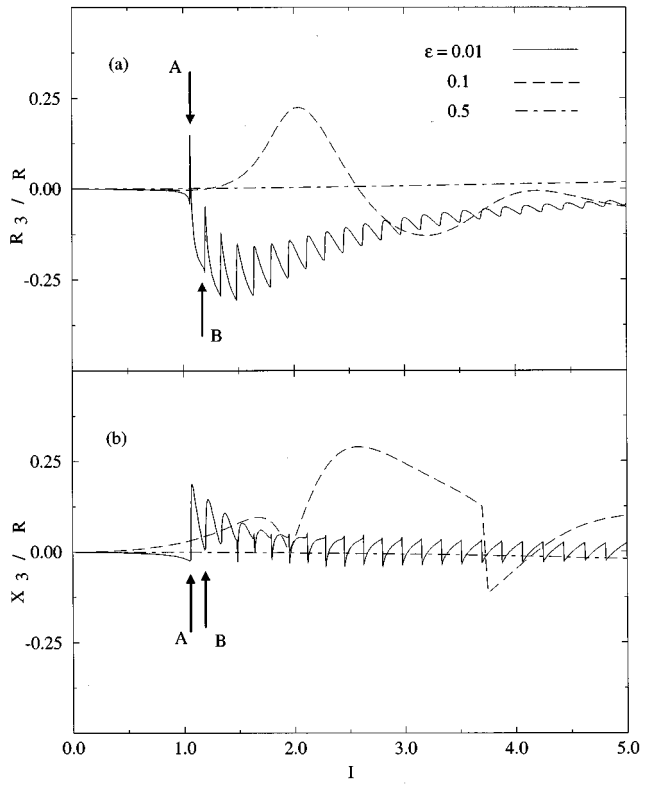

FIG. 4. The third harmonic responses R_3 (top) and X_3 (bottom) vs I in the RSJ model for the same three values of ε as in Fig. 3. When ε is small, there are very sharp oscillations. These oscillations, which occur because of bifurcations in the gauge-invariant phase difference $\Delta\gamma$, have a behavior similar to the behavior described in the caption to Fig. 3. Arrows indicate steps at values of I for which the bifurcations are shown in Fig. 5.

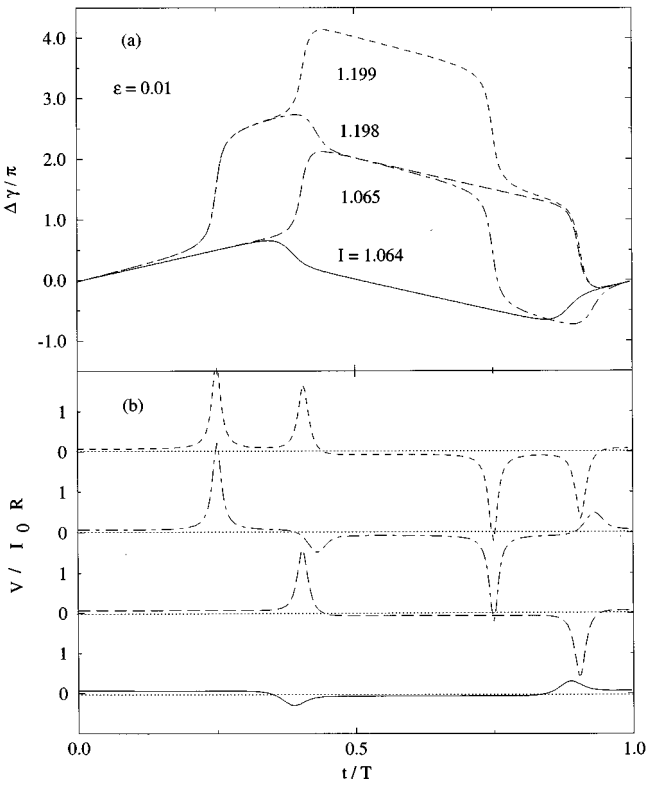

FIG. 5. Plots of the gauge-invariant phase difference $\Delta\gamma(t)$ (a) and voltage drop $V(t)=(\phi_0/2\pi)d\Delta\gamma(t)/dt$ (b) vs t, for $\varepsilon=0.01$, showing the first two bifurcations. The first bifurcation occurs between $I=1.064$ and $I=1.065$, and the second between $I=1.198$ and $I=1.199$. The bifurcations occur because $\Delta\gamma$ slips by 2π. For clarity, the voltage curves are offset in the vertical direction.

$$b_z(x,t)=-\frac{\phi_0}{2\pi d}\frac{\partial}{\partial x}\Delta\gamma(x,t). \tag{19}$$

The relation between $\Delta\gamma(x,t)$ and the electric field across the junction $e_y(x,t)$ is

$$e_y(x,t)=\frac{\phi_0}{2\pi d_i}\frac{\partial}{\partial t}\Delta\gamma(x,t). \tag{20}$$

The current density across the junction $J_y(x,t)$ is given by

$$J_y(x,t)=J_0\sin\Delta\gamma(x,t)+\frac{e_y(x,t)}{\rho_i}. \tag{21}$$

The first term is the Josephson relation for the supercurrent density and the second term is the normal leakage current density. $J_y(x,t)$ is related to $b_z(x,t)$ and $e_y(x,t)$ by Ampère's law with a displacement current,

$$-\frac{\partial}{\partial x}b_z(x,t)=\mu_0 J_y(x,t)+\mu_0\epsilon\frac{\partial}{\partial t}e_y(x,t). \tag{22}$$

By combining Eqs. (19)–(22), we obtain a single equation for $\Delta\gamma(x,t)$,

$$\frac{\partial^2}{\partial x'^2}\Delta\gamma(x',t')-\frac{1}{4\pi^2}\left(\frac{\omega}{\omega_p}\right)^2\frac{\partial^2}{\partial t'^2}\Delta\gamma(x',t')$$

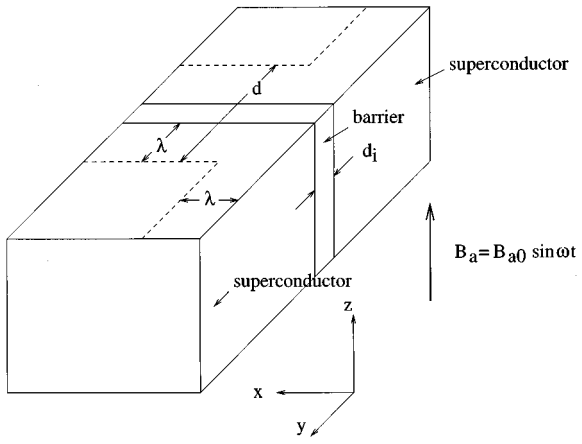

FIG. 6. Geometry of a long Josephson junction. The region $x>0$, excluding a slab of thickness d_i centered on the x-z plane, is occupied by a superconductor with London penetration depth λ. The slab-shaped barrier region is characterized by a resistivity ρ_i. An ac magnetic field B_a is applied parallel to the z axis. A weak field will penetrate into the superconductor a distance λ from the surface $x=0$. The length of penetration along the barrier region is given by $\lambda_J=\sqrt{\phi_0/2\pi\mu_0 J_0 d}$, where J_0 is the Josephson critical current density of the junction and $d=2\lambda+d_i$ is the magnetic thickness of the junction.

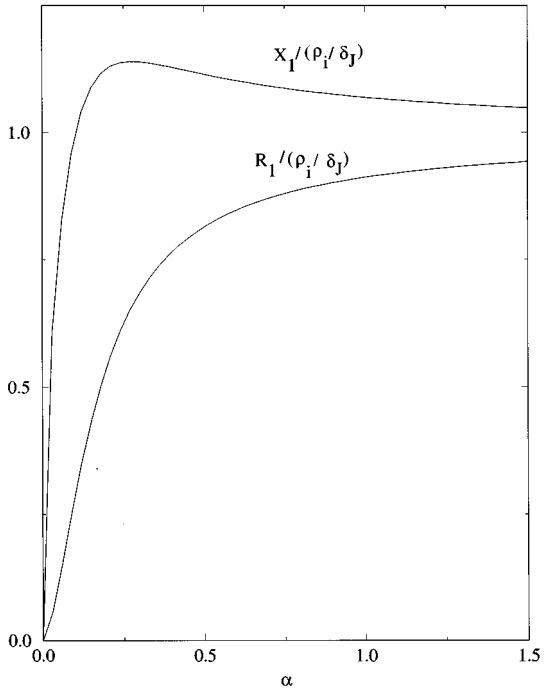

FIG. 7. Resistance R_1 and reactance X_1 of a long uniform junction vs damping parameter α for $F \ll 1$. R_1 increases from zero with increasing α and quickly approaches the limiting value ρ_i/δ_J. X_1 initially increases with increasing α up to a value larger than the limiting value ρ_i/δ_J, then slowly approaches the limiting value from above as $\alpha \to \infty$.

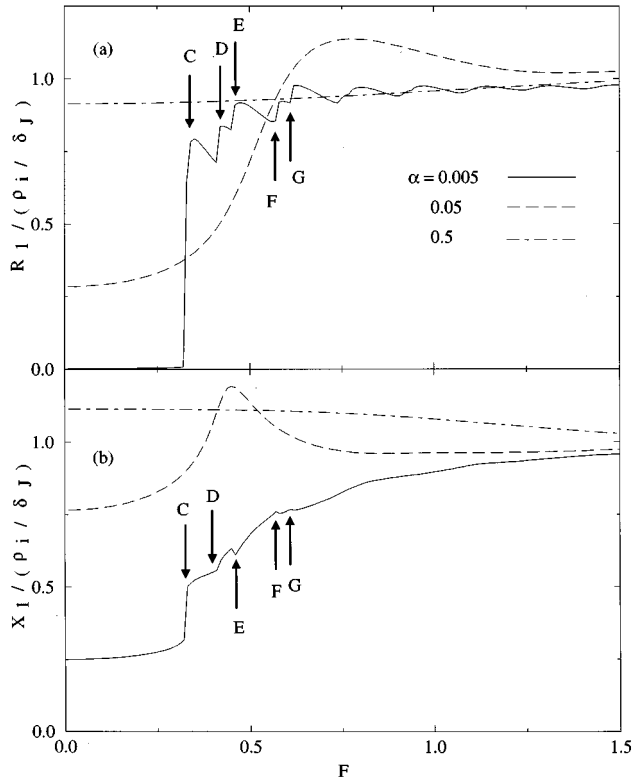

FIG. 8. Resistance R_1 (a) and reactance X_1 (b) of a long, uniform junction vs F for three different values of α. When α is small, sharp features (C, D, E, F, and G) are visible. These features occur because of changes in the number of Josephson vortices in the barrier region. As the damping parameter α increases, the threshold for vortex nucleation is pushed to larger values of F and the vortex dynamics play a less significant role. This causes the sharp features to become broadened and eventually to disappear completely.

$$-\alpha \frac{\partial}{\partial t'} \Delta\gamma(x',t') = \sin \Delta\gamma(x',t'), \tag{23}$$

where $x' = x/\lambda_J$, $t' = t/T = \omega t/2\pi$, $\omega_p = \sqrt{1/\mathcal{L}_J \mathcal{C}_J}$, $\alpha = \omega \mathcal{L}_J / 2\pi\rho_i d_i$, $\mathcal{C}_J = \epsilon/d_i$, and $\mathcal{L}_J = \phi_0/2\pi J_0$. There is also a boundary condition at $x' = 0$,

$$\left[\frac{\partial}{\partial x'} \Delta\gamma(x',t')\right]_{x'=0} = -2\pi F \sin(2\pi t'), \tag{24}$$

where $F = (B_{a0}\lambda_J d)/\phi_0$. The coefficient α is a damping parameter which arises because of the electrical connection between the superconductors. In the limit $\rho_i \to \infty$, $\alpha = 0$ and Eq. (23) reduces to the usual sine-Gordon equation.[21] The frequency ω_p is the plasma frequency of the junction and is usually in the infrared region of the spectrum ($\omega_p \simeq 10^{12}$ rad/s). For microwave applications $\omega \simeq 10^9$ rad/s,[10,13] and so $\omega \ll \omega_p$; therefore, Eq. (23) reduces to

$$\frac{\partial^2}{\partial x'^2} \Delta\gamma(x',t') - \alpha \frac{\partial}{\partial t'} \Delta\gamma(x',t') = \sin \Delta\gamma(x',t'). \tag{25}$$

The steady-state solution for $\Delta\gamma(x',t')$ is periodic in t' with period unity. The electric field given by Eq. (20) is also periodic with the same period. Therefore, $e_y(x'=0,t')$ may be expanded in a Fourier series,

$$e_y(0,t') = H_{a0} \sum_{n=1}^{\infty} [R_n \sin(2\pi n t') + X_n \cos(2\pi n t')], \tag{26}$$

where $H_{a0} = B_{a0}/\mu_0$, and the coefficients are given by

$$R_n = \frac{2}{H_{a0}} \int_0^1 e_y(0,t') \sin(2\pi n t') dt' \tag{27}$$

and

$$X_n = \frac{2}{H_{a0}} \int_0^1 e_y(0,t') \cos(2\pi n t') dt'. \tag{28}$$

By the Poynting theorem, the power per unit height absorbed by the surface $P'_{\rm abs}$ is given by

$$P'_{\rm abs} = \int_0^1 dt' \int_{-\infty}^{\infty} dy [\mathbf{E} \times \mathbf{H}]_{x'=0}. \tag{29}$$

The only nonzero contribution comes from the region $-d_i/2 < y < d_i/2$, where the electric field is given by Eq. (26). Inserting Eq. (26) into Eq. (29) yields

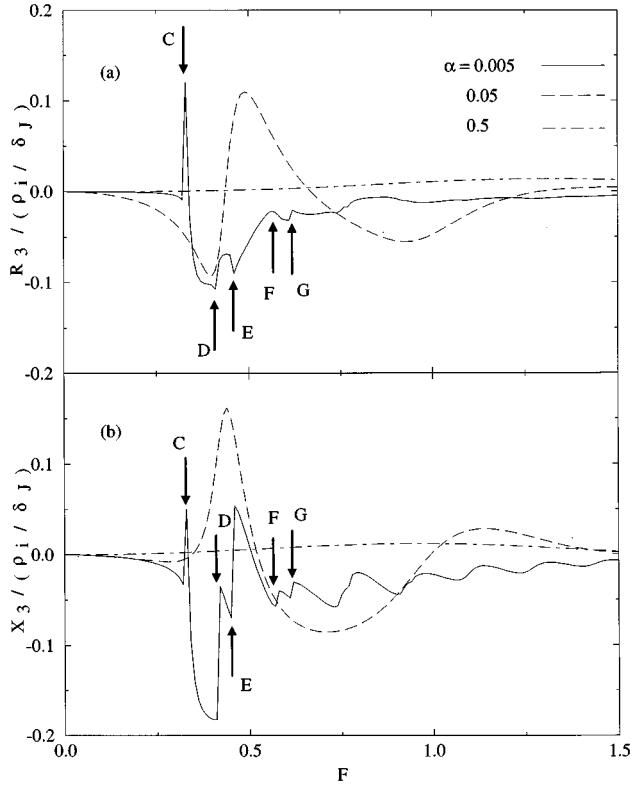

FIG. 9. Third harmonics R_3 (a) and X_3 (b) vs F for a long, uniform junction for three different values of α. When α is small, there are some sharp features (C, D, E, F, and G) visible that are associated with the nucleation of Josephson vortices in the barrier region. As α increases, the threshold for vortex nucleation is pushed to larger values of F and the vortex dynamics play a less significant role in the electrodynamic properties of the junction. This causes the sharp features to become smoother and eventually to disappear completely.

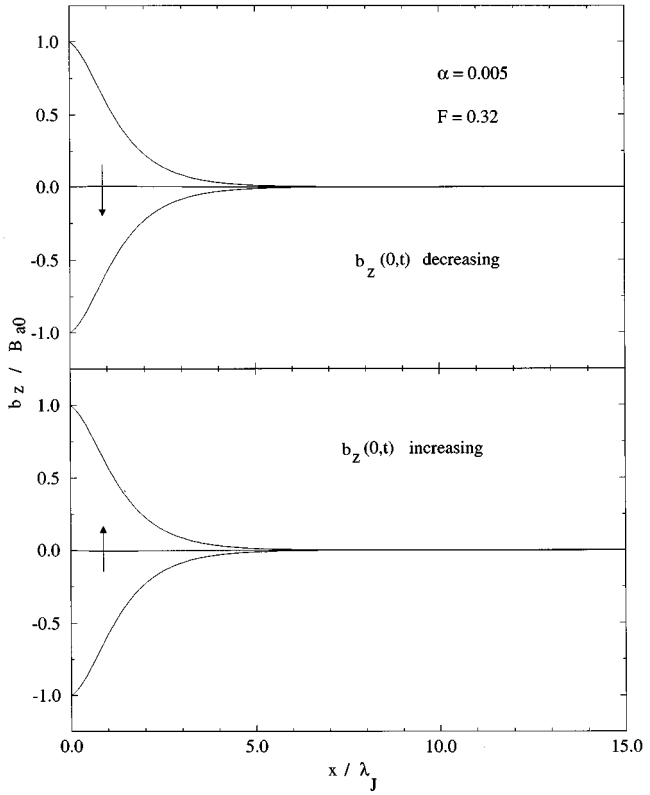

FIG. 10. Profiles of $b_z(x,t)$ versus x for a long uniform junction with $\alpha=0.005$ at $F=0.32$, just before the first vortex nucleation process will occur. The top figure corresponds to the external ac field decreasing from $+B_{a0}$ to $-B_{a0}$, and the bottom figure corresponds to the external ac field increasing from $-B_{a0}$ to $+B_{a0}$. The external field is screened by the junction on a scale of a few λ_J.

$$P'_{\rm abs}=\frac{1}{2}d_i H_{a0}^2 R_1, \tag{30}$$

which implies that R_1 is proportional to the surface resistance R_s. If the length of the sample in the y direction is equal to L, or if there is an array of long junctions spaced along the y direction with periodicity length L, then $R_s=(d_i/L)R_1$. We ignore here the energy dissipated via quasiparticles (normal fluid) within λ of the surface of the superconductor. Similarly, the surface reactance X_s is given by $X_s=(d_i/L)X_1+(1-d_i/L)\mu_0\omega\lambda$. The second term in X_s is due to the electric fields that accelerate the screening currents near the surface of the superconductor.

In the limit of small applied field, $F\ll 1$, $\sin\Delta\gamma\simeq\Delta\gamma$, and Eq. (25) can be linearized,

$$\frac{\partial^2}{\partial x'^2}\Delta\gamma(x',t')-\alpha\frac{\partial}{\partial t'}\Delta\gamma(x',t')-\Delta\gamma(x',t')=0, \tag{31}$$

with the boundary condition given by Eq. (24). The steady-state solution for $\Delta\gamma(x',t')$ is

$$\Delta\gamma(x',t')=-\frac{2\pi F}{a^2+b^2}e^{-ax'}[a\ \sin(bx'-2\pi t') + b\ \cos(bx'-2\pi t')], \tag{32}$$

where

$$a=(1+4\pi^2\alpha^2)^{1/4}\cos\left(\frac{1}{2}\tan^{-1}(2\pi\alpha)\right) \tag{33}$$

and

$$b=(1+4\pi^2\alpha^2)^{1/4}\sin\left(\frac{1}{2}\tan^{-1}(2\pi\alpha)\right). \tag{34}$$

The electric field at the surface is given by

$$e_y(0,t')=H_{a0}\frac{\rho_i}{\lambda_J}\frac{2\pi\alpha}{a^2+b^2}[a\ \cos(2\pi t')+b\ \sin(2\pi t')], \tag{35}$$

so that

$$R_1=\frac{\rho_i}{\lambda_J}\frac{2\pi\alpha b}{a^2+b^2}=\frac{\rho_i}{\lambda_J}\frac{2\pi\alpha}{(1+4\pi^2\alpha^2)^{1/4}}\sin\left(\frac{1}{2}\tan^{-1}(2\pi\alpha)\right) \tag{36}$$

and

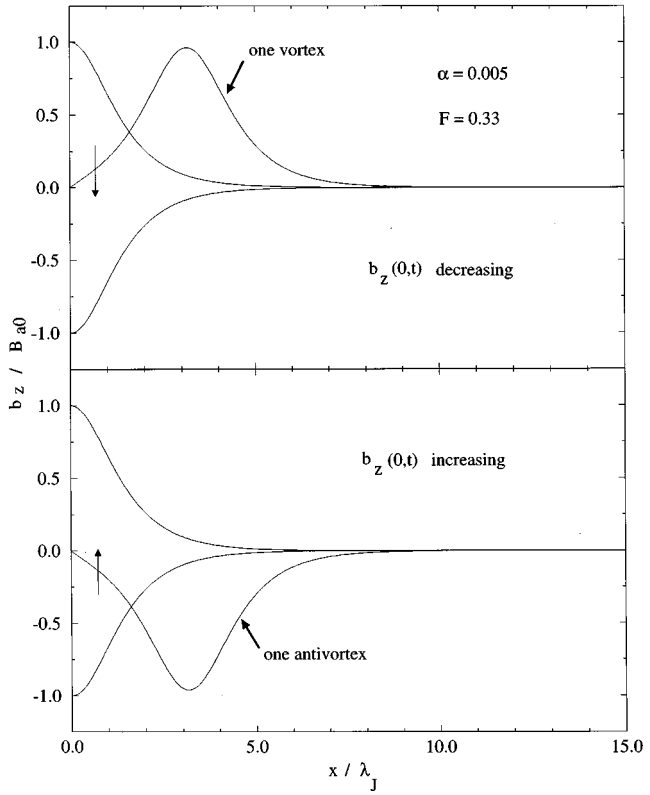

FIG. 11. Profiles of $b_z(x,t)$ vs x for a long, uniform junction with $\alpha=0.005$ at $F=0.33$, just after the first vortex nucleation process (feature C in Figs. 8 and 9) has occurred. The top figure corresponds to the external ac field decreasing from $+B_{a0}$ to $-B_{a0}$. The bottom figure corresponds to the external ac field increasing from $-B_{a0}$ to $+B_{a0}$. When the external field is zero, there is clearly either a vortex (top figure) or an antivortex (bottom figure) trapped in the junction. The field-increasing and field-decreasing profiles of $b_z(x)$ are mirror images of each other.

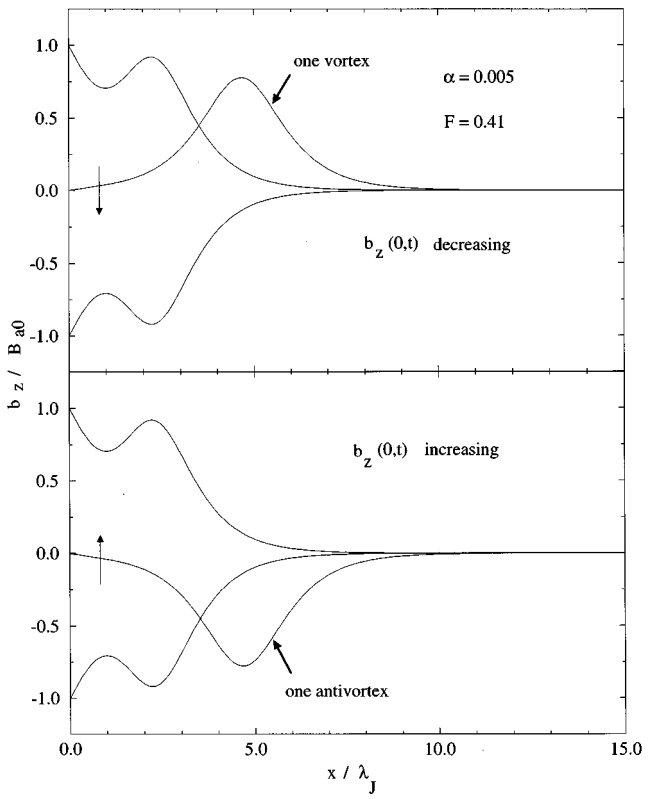

FIG. 12. Profiles of $b_z(x,t)$ vs x for a long uniform junction with $\alpha=0.005$ at $F=0.41$, just before the second vortex nucleation process (feature D in Figs. 8 and 9) will occur. The top figure corresponds to the external ac field decreasing from $+B_{a0}$ to $-B_{a0}$. The bottom figure corresponds to the external ac field increasing from $-B_{a0}$ to $+B_{a0}$. When the external field is zero there is clearly either a vortex (top figure) or an antivortex (bottom figure) trapped in the junction.

$$X_1=\frac{\rho_i}{\lambda_J}\frac{2\pi\alpha a}{a^2+b^2}=\frac{\rho_i}{\lambda_J}\frac{2\pi\alpha}{(1+4\pi^2\alpha^2)^{1/4}}\cos\left(\frac{1}{2}\tan^{-1}(2\pi\alpha)\right). \tag{37}$$

Figure 7 shows R_1 and X_1 as functions of α. In the opposite limit of large applied field, $F\gg 1$, $e_y(x',t')/\rho_i\gg J_0\sin\Delta\gamma(x',t')$, and Eq. (25) becomes

$$\frac{\partial^2}{\partial x'^2}\Delta\gamma(x',t')=\alpha\frac{\partial}{\partial t'}\Delta\gamma(x',t'), \tag{38}$$

with the boundary condition given by Eq. (24). The solution for $\Delta\gamma(x',t')$ is

$$\Delta\gamma(x',t')=-F\sqrt{\frac{\pi}{\alpha}}\,e^{-\sqrt{\pi\alpha}x'}[\sin(\sqrt{\pi\alpha}x'-2\pi t') +\cos(\sqrt{\pi\alpha}x'-2\pi t')], \tag{39}$$

which gives

$$e_y(0,t')=H_{a0}\frac{\rho_i}{\lambda_J}\sqrt{\pi\alpha}e^{-\sqrt{\pi\alpha}x'}[\cos(2\pi t')+\sin(2\pi t')] \tag{40}$$

and

$$R_1=X_1=\frac{\rho_i}{\delta_J}, \tag{41}$$

where we have defined the Josephson skin depth $\delta_J=\lambda_J/\sqrt{\pi\alpha}=(2\rho_i d_i/\mu_0 d\omega)^{1/2}$. This is also the result for the limit of large damping, $\alpha\gg 1$. Thus, at high fields or large damping the junction behaves like a normal metal with resistivity ρ_i and skin depth δ_J. The reason for this is that in these two limits the magnitude of the normal current is much larger than the magnitude of the supercurrent, and the normal current, therefore, dominates the behavior of the junction.

In general Eq. (25) must be solved numerically. Figure 8(a) shows R_1 versus F for three different values of α. For the smallest value of α, there are sharp jumps in R_1 (C, D, and E for example) which decrease in amplitude as F increases. For $F\gtrsim 1$, R_1 quickly approaches the saturation value ρ_i/δ_J. As α increases, the sharp steps become broader until they disappear completely and R_1 approaches ρ_i/δ_J for all values of F. From Fig. 10(a), below, it is apparent that this limit is approached even for very modest values of α. The behaviors of X_1, R_3, and X_3 vs F for the same values of α are shown in Figs. 8(b), 9(a), and 9(b), respectively.

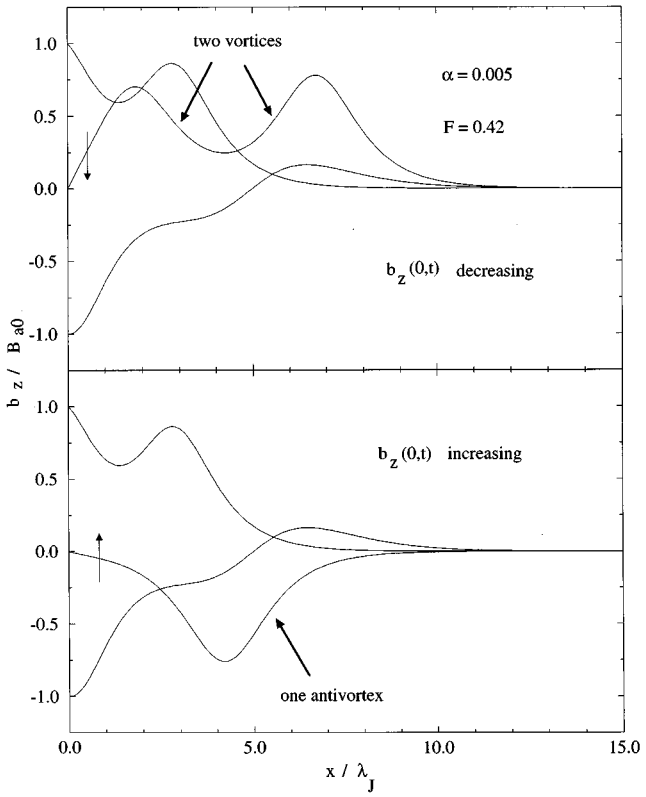

FIG. 13. Profiles of $b_z(x,t)$ vs x for a long uniform junction with $\alpha=0.005$ at $F=0.42$, just after the second vortex nucleation process (feature D in Figs. 8 and 9) has occurred. The top figure corresponds to the external ac field decreasing from $+B_{a0}$ to $-B_{a0}$. The bottom figure corresponds to the external ac field increasing from $-B_{a0}$ to $+B_{a0}$. When the external field is zero, there is clearly either a pair of vortices (top figure) or a single antivortex (bottom figure) trapped in the junction. The field-increasing and field-decreasing profiles of $b_z(x)$ are no longer mirror images of each other.

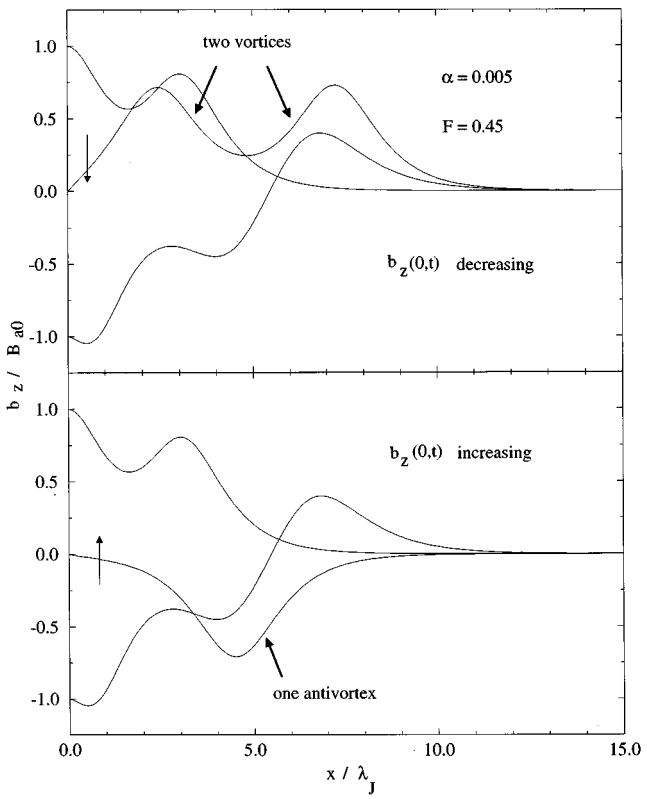

FIG. 14. Profiles of $b_z(x,t)$ vs x, for a long uniform junction with $\alpha=0.005$ at $F=0.45$, just before the third vortex nucleation process (feature E in Figs. 8 and 9) will occur. The top figure corresponds to the external ac field decreasing from $+B_{a0}$ to $-B_{a0}$. The bottom figure corresponds to the external ac field increasing from $-B_{a0}$ to $+B_{a0}$. When the external field is zero there is clearly either a pair of vortices (top figure) or a single antivortex (bottom figure) trapped in the junction, and the field-increasing and field-decreasing profiles of $b_z(x)$ still are not mirror images of each other.

The sharp jumps and fine features (C, D, E, F, and G) in Figs. 8 and 9 for $\alpha=0.005$ are caused by changes in the number of Josephson vortices in the junction. The nucleation of a vortex at the first jump (C) in R_1 is depicted in Figs. 10 and 11. Several field profiles are shown as the field at the surface changes through one period. Just below the jump C shown in Figs. 8 and 9 ($F=0.32$) the field decays from the surface (see Fig. 10) and there are no vortices visible. However, just above this jump ($F=0.33$) (Fig. 11), there is clearly a vortex trapped in the junction during one half cycle and an antivortex trapped during the other half cycle. The nucleation process at the second jump (D in Figs. 8 and 9) is shown in Figs. 12 and 13. Just below the jump ($F=0.41$) there is either a single vortex or a single antivortex inside the junction. Just above the jump ($F=0.42$) there are two vortices trapped during one half cycle but only one antivortex trapped during the other half cycle. At the third jump (E in Figs. 8 and 9), the symmetry between the two half cycles is restored, so that there is a two-vortex–two-antivortex state (Figs. 14 and 15). There is another shift to an asymmetric three-vortex–two-antivortex state at the fourth jump (F in Figs. 8 and 9), and the symmetry is then restored to a three-vortex–three-antivortex state at the fifth jump (G in Figs. 8 and 9). The asymmetry occurring between the second and third jumps (D and E in Figs. 8 and 9), and between the fourth and fifth jumps (F and G in Figs. 8 and 9), leads to the generation of second harmonics, as shown in Fig. 16. The signs of R_2 and X_2 depend on whether the jump is approached from below (increasing F) or above (decreasing F). This effect occurs because the direction that the symmetry is broken (more vortices than antivortices or vice versa) depends on the previous history of the junction.

IV. JOSEPHSON JUNCTION ARRAYS

Josephson junction arrays have been studied previously by various authors.[34–36] Here we offer only a brief summary of some of the previous work in order to compare it with the results of this paper.

Consider a three-dimensional cubic lattice of isotropic superconducting grains, with lattice spacing a. For simplicity we assume that the grain size is smaller than the London penetration depth characterizing each grain, so that we may neglect the effects of intragranular screening currents.[18] Each

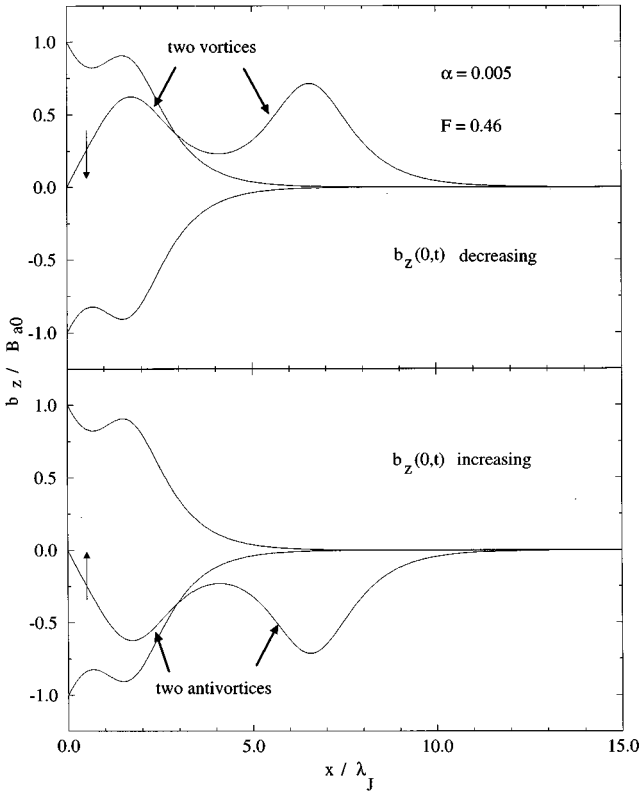

FIG. 15. Profiles of $b_z(x,t)$ vs x for a long uniform junction with $\alpha=0.005$ at $F=0.46$, just after the third vortex nucleation process (feature E in Figs. 8 and 9) has occurred. The top figure corresponds to the external ac field decreasing from $+B_{a0}$ to $-B_{a0}$. The bottom figure corresponds to the external ac field increasing from $-B_{a0}$ to $+B_{a0}$. When the external field is zero there is clearly either a pair of vortices (top figure) or a pair of antivortices (bottom figure) trapped in the junction, and the field-increasing and field-decreasing profiles of $b_z(x)$ again are mirror images of each other.

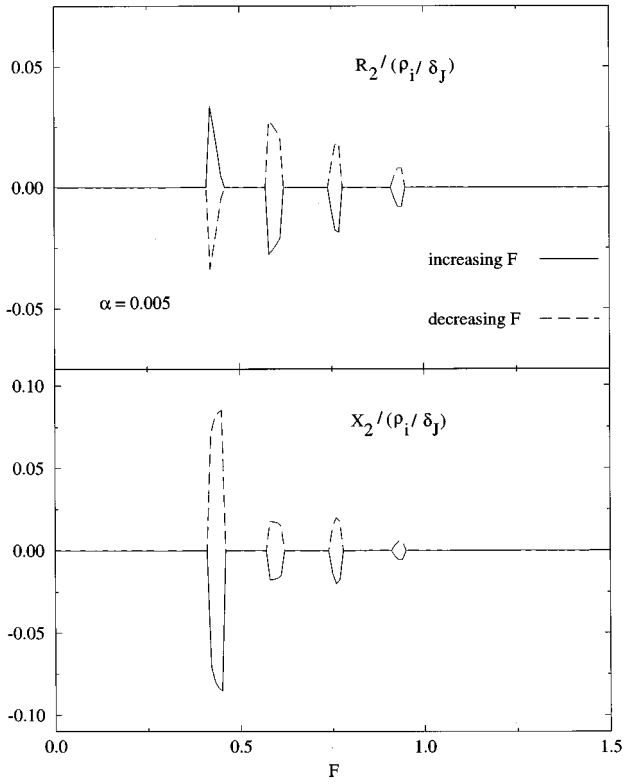

FIG. 16. Second harmonics R_2 and X_2 vs F, for a long uniform junction with $\alpha=0.005$. These harmonics are generated by the asymmetry in the field profiles between the two half periods of oscillation of the external field, as illustrated in Figs. 13 and 14. The sign of these harmonics depends on whether it is a vortex nucleation process (increasing F) or a vortex exit process (decreasing F). The difference in sign occurs because the direction of the asymmetry (more vortices than antivortices or vice versa) depends on the previous history of the junction.

grain is coupled to each of its nearest neighbors by a Josephson junction with coupling energy $E_J=\phi_0 I_0/2\pi$. We may define a macroscopic critical current density $J_0=I_0/a^2$. The response of the array to a weak magnetic field is Meissner like with a screening length $\lambda_J=\sqrt{\phi_0/2\pi\mu_0 a J_0}$.[18,20–22] For a weakly coupled array $\lambda_J \gg a$, and the array can be approximated as a continuous medium from the standpoint of its electromagnetic response. In this limit, Josephson fluxons will penetrate the sample when the applied field reaches the value $H_{c1J}=(\phi_0/4\pi\lambda_J^2)\ln(\lambda_J/\xi_J)$ where $\xi_J \simeq a/2$.[18,20,21]

In the limit of strong Josephson coupling between the grains, $\lambda_J \ll a$ and the discrete nature of the array becomes very important. For weak fields, the array will be screened from the applied field. When the applied field becomes large enough, flux will begin to penetrate in from the surface. The characteristic size of a Josephson vortex is λ_J, which in this limit is much smaller than the plaquette size. Therefore, the concept of a Josephson vortex is not very useful for strongly coupled arrays.[35]

Instead we may think in terms of elementary excitations that consist of a phase change of 2π when the contour encircling a flux penetrated plaquette is traversed. The number of excitations in a given plaquette is equal to the number of flux quanta that are trapped in it. Because of the discrete nature of the array, there is a pinning energy proportional to E_J associated with these excitations.[34] It has been demonstrated numerically that these excitations form a critical state analogous to the Bean critical state in a type-II superconductor.[35,36] The surface resistance and reactance for the Bean model are $R_s=(2\omega B_{a0}/3\pi J_c)$ and $X_s=(\omega B_{a0}/2J_c)$, where J_c is the macroscopic critical current density. This limit has been studied experimentally by Fisher *et al.*[37]

V. SUMMARY

We have analyzed the response of both small and long, uniform Josephson junctions to ac fields or currents with frequencies much smaller than the Josephson plasma frequency. In both cases the behavior of the junction was found to be strongly dependent on the strength of the resistive damping. For small damping, sharp features were found in the resistive, reactive, and higher-harmonic responses as a function of the ac field amplitude. In the case of small junctions, the sharp features are caused by bifurcations, or 2π

phase slips, in the gauge-invariant phase difference across the junction. In the case of long, uniform junctions, the sharp features are due to changes in the number of Josephson vortices in the junction. For both small and long, uniform junctions the resistive response saturates at large ac current amplitudes I_{T0} or ac field amplitudes B_{a0}. This behavior is in contrast to a strongly coupled Josephson array which behaves like a type-II superconductor in the Bean critical state with a surface resistance that grows linearly with B_{a0}.

Some of the vortex nucleation processes in long, uniform junctions were found to create asymmetric field profiles between the two half periods of oscillation of the external field. These asymmetric field profiles lead to the generation of second harmonics. The signs of the second harmonics for decreasing applied field were found to be opposite to those for increasing applied field.

ACKNOWLEDGMENTS

Ames Laboratory is operated for the U.S. Department of Energy by Iowa State University under Contract No. W-7405-Eng-82. This research was supported by the Director for Energy Research, Office of Basic Energy Sciences.

[1] S. Shapiro, Phys. Rev. Lett. **11**, 80 (1963).
[2] V. Ambegaokar and B. I. Halperin, Phys. Rev. Lett **22**, 1364 (1969).
[3] M. Sheuermann, J. T. Chen, and J. Chang, J. Appl. Phys. **54**, 3286 (1983).
[4] B. A. Huberman, J. P. Crutchfield, and N. H. Packard, Appl. Phys. Lett. **37**, 750 (1980).
[5] A. H. MacDonald and M. Plischke, Phys. Rev. B **27**, 201 (1983).
[6] T. Jacobs, B. A. Willemsen, S. Sridhar, Qiang Li, G. D. Gu, and N. Koshizuka, *Tenth Annivesary HTS Workshop on Physics, Materials and Applications* (World Scientific, Singapore, 1996).
[7] T. Jacobs, B. A. Willemsen, and S. Sridhar, Rev. Sci. Instrum. **67**, 3757 (1996).
[8] J. S. Herd, D. E. Oates, and J. Halbritter (unpublished).
[9] L. M. Xie, J. Wosik, and J. C. Wolfe, Phys. Rev. B **54**, 15 494 (1996).
[10] G. B. Lubkin, Phys. Today **48**(3), 20 (1995).
[11] D. E. Oates, P. P. Nguyen, G. Dresselhaus, M. S. Dresselhaus, G. Koren, and E. Polturak, J. Supercond. **8**, 725 (1995).
[12] G.-C. Liang, D. Zhang, C.-F. Shih, M. E. Johansson, R. S. Withers, W. Ruby, D. E. Oates, A. C. Anderson, P. A. Polakos, P. M. Mankiewich, E. DeObaldia, and R. E. Miller, IEEE Trans. Microwave Theory Tech. **43**, 3020 (1995).
[13] Z.-Y. Shen, *High-Temperature Superconducting Microwave Circuits* (Artech House, Boston, 1994).
[14] S. E. Babcock and J. L. Vargas, Annu. Rev. Mater. Sci. **25**, 193 (1995).
[15] T. C. L. Gerhard Sollner, J. P. Sage, and D. E. Oates, Appl. Phys. Lett. **68**, 1003 (1996).
[16] D. E. Oates, P. P. Nguyen, Y. Habib, G. Dresselhaus, M. S. Dresselhaus, G. Koren, and E. Polturak, Appl. Phys. Lett. **68**, 705 (1996).
[17] P. P. Nguyen, D. E. Oates, G. Dresselhaus, M. S. Dresselhaus, and A. C. Anderson, Phys. Rev. B **51**, 6686 (1995).
[18] J. R. Clem, Physica C **153-155**, 50 (1988).
[19] H. Dersch and G. Blatter, Phys. Rev. B **38**, 11 391 (1988).
[20] M. Tinkham and C. J. Lobb, Solid State Phys. **42**, 91 (1989).
[21] M. Tinkham, *Introduction to Superconductivity*, 2nd ed. (McGraw-Hill, New York, 1996).
[22] E. B. Sonin and A. K. Tagantsev, Phys. Lett. A **140**, 127 (1989).
[23] T. L. Hylton, A. Kapitulnik, M. R. Beasley, J. P. Carini, L. Drabeck, and G. Gruner, Appl. Phys. Lett. **53**, 1343 (1988).
[24] C. Attanasio, L. Maritato, and R. Vaglio, Phys. Rev. B **43**, 6128 (1991).
[25] P. P. Nguyen, D. E. Oates, G. Dresselhaus, and M. S. Dresselhaus, Phys. Rev. B **48**, 6400 (1993).
[26] M. Mahel, Solid State Commun. **97**, 209 (1996).
[27] J. Halbritter, J. Appl. Phys. **68**, 6315 (1990).
[28] J. Halbritter, J. Appl. Phys. **71**, 339 (1992).
[29] J. Halbritter, J. Supercond. **8**, 691 (1994).
[30] T. Van Duzer and C. W. Turner, *Principles of Superconductive Devices and Circuits* (Elsevier, New York, 1981).
[31] S. Sridhar (unpublished).
[32] M. Perpeet, M. A. Hein, H. Piel, S. Beuven, M. Siegel, and E. Sodtke (unpublished).
[33] F. Auracher and T. Van Duzer, J. Appl. Phys. **44**, 848 (1973).
[34] C. J. Lobb, D. W. Abraham, and M. Tinkham, Phys. Rev. B **27**, 150 (1983).
[35] D.-X. Chen, A. Hernando, and A. Sanchez, Physica C **250**, 107 (1995).
[36] M. Chandran and P. Chaddah, Physica C **267**, 59 (1996).
[37] L. M. Fisher, V. S. Gorbachev, N. V. Il'in, N. M. Makarov, I. F. Voloshin, V. A. Yampol'skii, R. L. Snyder, S. T. Misture, M. A. Rodriguez, D. P. Matheis, V. R. W. Amarakoon, J. G. Fagan, J. A. T. Taylor, and A. M. M. Barus, Phys. Rev. B **46**, 10 986 (1992).